A Degenerate Point Index

In this section, we provide detail of our theoretical analysis on the index of degenerate points in a 3D symmetric tensor field (Section 4.2).

Let R be a topological disk without self-intersections such that there are no degenerate points on its boundary, ∂R (the circles in Figure 7 (a-b)). We consider the right-handed frames formed by the unit major eigenvector v_1, the medium eigenvector v_2, and the minor eigenvector v_3 of the tensor fields on ∂R. There are four ways of selecting a right-handed frame from the eigenvectors. Let $f_0(p) = (v_1, v_2, v_3)$ be one such frame. Then $f_1(p) = (v_1, -v_2, -v_3)$, $f_2(p) = (-v_1, v_2, -v_3)$, and $f_3(p) = (-v_1, -v_2, v_3)$ are the other choices of such frames (Figure 7 (left)). Let r_m ($0 \le m \le 3$) be the 3D rotation that maps the X-axis to the major eigenvector in $f_m(p)$, the Y-axis to the medium eigenvector, and the Z-axis to the minor eigenvector (Figure 7 (left)). Define r_x, r_y, and r_z as the 180° rotation around the X-, Y-, and Z-axis, respectively. Then we have

$$r_1 = r_0 r_x \quad (9)$$
$$r_2 = r_0 r_y \quad (10)$$
$$r_3 = r_0 r_z \quad (11)$$

We choose $p_0 \in \partial R$ and travel along ∂R for one round in order to inspect the behavior of the *continuous* eigenframe that is initially set to be $f_0(p_0)$ (Figure 7 (a-b)). Since the tensor field is continuous over R and there is no degenerate point on ∂R, we know that the eigenvector fields are also continuous over ∂R. Therefore, when returning to p_0 after a full boundary walk, the frame $f'(p_0)$ must be $f_m(p_0)$ for some $0 \le m \le 3$. That is,

$$r'(p_0) = r_0(p_0)c \quad (12)$$

where $c = 1$, r_x, r_y, or r_z. Thus $c = r_0(p_0)^{-1} r'(p_0)$. Next, we show that c is a curve invariant.

Lemma 1. *Given the conditions above, c is independent of the coordinate system for the space.*

Proof. Let S and T be two right-handed orthogonal coordinate systems (Figure 14). Let P be the change-of-basis matrix from T to S. Note that P^{-1} can also be considered as the rotation that takes the coordinate system S to the coordinate system T.

Therefore, $r_{0,S}(p_0)$, the rotation that takes S to the eigenframe $f_0(p_0)$, is related to $r_{0,T}(p_0)$, the rotation that takes the T to the eigenframe $f_0(p_0)$, as follows: $r_{0,S}(p_0) = r_{0,T}(p_0)P^{-1}$. Similarly, $r'_S(p_0) = r'_T(p_0)P^{-1}$.

We now consider $c_S = (r_{0,S}(p_0))^{-1} r'_S(p_0)$. This is equivalent to $c_S = (r_{0,T}(p_0)P^{-1})^{-1} r'_T(p_0)P^{-1} = P(r_{0,T}(p_0))^{-1} r'_T(p_0)P^{-1} = Pc_T|_S P^{-1}$.

We consider the matrices corresponding to c_S and c_T under S. Thus, $c_S|_S = P|_S(c_T|_S)P^{-1}|_S$. Since $P|_S$ and $P|_S^{-1}$ commute, we have $P|_S = P|_T$ and $P^{-1}|_S = P^{-1}|_T$. Thus, we drop the subscripts and only use P and P^{-1}. On the other hand, $c_T|_S = P^{-1}(c_T|_T)P$. Thus, $c_S|_S = P(c_T|_S)P^{-1} = P(P^{-1}(c_T|_T)P)P^{-1} = c_T|_T$.

Therefore, c is independent of the choice of the coordinate system. □

Lemma 2. *Given the conditions above, c is independent of the initial frame chosen.*

Proof. Assume that we have chosen $f_m(p_0)$ as the initial frame where $m \neq 0$. Let p_1, ... p_n be a sequence of points on ∂R in the direction of the travel such that $p_n = p_0$ (Figure 7 (a-b)). Moreover, we choose the sample points so that at each sample point p_ℓ, there is a unique k_0 that minimizes $d(f_0(p_\ell), f_k(p_{\ell+1}))$, the distance between the two frames (the angle of the minimal 3D rotation that takes the first frame to the second frame). For convenience, we reorder the four frames at $p_{\ell+1}$ such that $f_{k_0}(p_{\ell+1})$ becomes $f_0(p_{\ell+1})$. Under the new numberings, we define $s_{\ell+1}$ to be the unique rotation that takes the frame $f_0(p_\ell)$ to $f_0(p_{\ell+1})$. That is, $s_\ell = r_0(p_{\ell+1})(r_0(p_\ell))^{-1}$. Note that $s_\ell(f_m(p_\ell)) = f_0(p_{\ell+1})$ for $1 \le m \le 3$. Therefore,

$$r'_m(p_0) = s_n s_{n-1} .. s_1 r_m(p_0) = s_n s_{n-1} .. s_1 r_0(p_0)c = r'(p_0)c \quad (13)$$

Consequently, $c' = (r_m(p_0))^{-1} r'_m(p_0) = c^{-1}(r_0(p_0))^{-1} r'(p_0)c = c^{-1}cc = c$. Thus, c does not depend on the choice of the initial frame. □

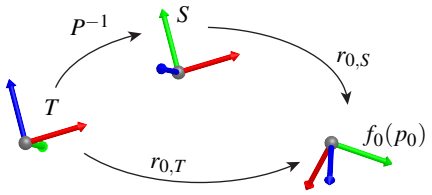

Fig. 14: This figure illustrates the change of the basis of S, T, and $f_0(p_0)$.

Lemma 3. *Given the conditions above, c is independent of the direction of travel along ∂R.*

Proof. Assume that we have chosen $f_0(p_0)$ as the initial frame. Let p_1, ... p_n be the sequence of points on ∂R from Lemma 2 (Figure 7 (a-b)). Furthermore, let $s_\ell = r_0(p_{\ell+1})(r_0(p_\ell))^{-1}$ be the unique rotation that takes the frame $f_0(p_\ell)$ to $f_0(p_{\ell+1})$. Then we have $s_\ell^{-1}(f_m(p_{\ell+1})) = f_0(p_\ell)$ for $1 \le \ell \le n$ and $0 \le m \le 3$.

We now consider travelling in the opposite direction along ∂R, that is, p_0, $p'_1 = p_{n-1}$, ... $p'_{n-1} = p_1$ and $p'_n = p_0$. Therefore, $c' = (r_0(p_0))^{-1} s_n^{-1} ... s_1^{-1} r_0(p_0) = ((r_0(p_0))^{-1} s_1 ... s_n r_0(p_0))^{-1} = (r_0(p_0))^{-1} r'(p_0))^{-1} = c^{-1} = c$.

Thus, c does not depend on the travel direction. □

Lemma 4. *Given the conditions above, c is independent of the choice of the starting point p_0.*

Proof. Let $p_0 \neq p'_0$ be two points on ∂R. Choose $f_0(p_0)$ as the initial frame. Let p_1, ... p_n be a sequence of points on ∂R described in Lemma 2 (Figure 7 (a-b)). Moreover, assume that $p_k = p'_0$ for some $1 \le k < n$. Using the process described Lemma 2, we can find $f_0(p'_0)$ such that $r_0(p'_0) = s_k s_{k-1} ... s_1 r_0(p_0)$.

We now consider travelling starting from p'_0 in the sequence of $p_{k+1}, .. p_{n-1}, p_0, ... p_{k-1}, p_k = p'_0$. Then, $r'(p'_0) = s_k s_{k-1} ... s_1 s_n ... s_{k+2} s_{k+1} r_0(p'_0)$. Therefore, $c' = (r_0(p'_0))^{-1} r'(p'_0) = (s_k s_{k-1} ... s_1 r_0(p'_0))^{-1} (s_k s_{k-1} ... s_1 s_n ... s_{k+2} s_{k+1} r_0(p'_0)) = (r_0(p_0))^{-1} s_n ... s_{k+1} r_0(p'_0) = (r_0(p_0))^{-1} s_n ... s_{k+1}(s_k .. s_1 r_0(p_0)) = c$.

Therefore, c does not depend on the choice of the initial point p_0. □

Lemma 5. *Given two topological disks R_1 and R_2 that intersect only at their common boundary such that $R_1 \bigcup R_2$ is still a topological disk, the winding number of the boundary of $R_1 \bigcup R_2$ is the product of the winding numbers of R_1 and R_2.*

Proof. Note that the boundary $\partial(R_1 \bigcup R_2) = \partial R_1 \bigcup \partial R_2$. Let $p_0 \in \partial R_1 \bigcap \partial R_2$ be the starting point and travel the boundary of $R_1 \bigcup R_2$. This is equivalent to traveling around the boundary of R_1 and R_2 once each, passing through p_0 once before returning to it a second time. Since the quaternion of a 3D rotation from concatenating two 3D rotations is the product of the quaternions for the two 3D rotations, the winding number of the boundary of $R_1 \bigcup R_2$ is the product of the respective winding numbers of the boundary of R_1 and the boundary of R_2. □

Lemma 6. *Given a 3D tensor field $T(x,y,z)$ and R, a topological ball on which $T(x,y,z)$ is linear, the major eigenvector field of $T(x,y,z)$, a 3D line field, can be turned into a 3D vector field inside R. Similarly, if $T(x,y,z)$ is planar on R, then the minor eigenvector field of $T(x,y,z)$ can be turned into a 3D vector field.*

Proof. Since R is a topological ball, it is simply connected and finite. If $T(x,y,z)$ is linear on R, the major eigenvector field is always well-defined in R, i.e., without singularities. Thus, it can be turned into a 3D vector field from the result of Markus [20], which states that a 3D line field can be turned into a 3D vector field on a simply-connected, finite region if the line field does not have any singularities in the region. The proof for the minor eigenvector field in planar regions is similar. □

Theorem 7. *Given a 3D tensor field $T(x,y,z)$ and a point p_0 (possibly a degenerate point), there exists a small enough neighborhood R of p_0 such that any topological disk inside R has the same winding number for its boundary if the disk contains p_0 but no other degenerate points of $T(x,y,z)$ and has no self-intersection. In this case, the winding number is $\mathbf{i}$ if p_0 is a linear wedge, $-\mathbf{i}$ if p_0 is a linear trisector, $\mathbf{k}$ if p_0 is planar wedge, $-\mathbf{k}$ if p_0 is planar trisector, and $\mathbf{1}$ if p_0 is not a degenerate point.*

Proof. If p_0 is a linear degenerate point, then there exists a neighborhood R of p_0 such that the major eigenvector field of $T(x,y,z)$ can be converted to a continuous vector field inside R without singularities (Lemma 6). According to the Flow Box theorem [2], there exists a region $R' \subset R$ and a diffeomorphism ϕ from R' to another space F such that the major eigenvector field (now a vector field on R') to a constant vector field defined on F. Without loss of generality, we can assume that the major eigenvector at p_0 has the same length as its image under ϕ, i.e., a 3D rotation without scaling. Since ϕ is a diffeomorphism, it is continuous. Therefore, it is possible to find an even smaller set $R'' \subset R'$ such that the diffeomorphism ϕ inside R'' can be approximated by $\phi(p_0)$ with a sufficiently small error ε. Notice that under ϕ, the tensor field $T' = \phi(T(x,y,z))$ is also a tensor field whose major eigenvectors are all parallel. In addition, $\phi(p_0)$ is a linear degenerate point of T'. Similarly, a topological disk D containing p_0 will be mapped to a topological disk containing $\phi(p_0)$. When ε is small enough, the winding number of the boundary of D is the same as the winding number of the boundary of $\phi(D)$ since $\phi(p_0)$ is a 3D rotation on the eigenvectors of the tensor field. We can further select R'' to be small enough such that any loop inside R'' is close to being planar, i.e., contained in some plane. Consequently, the image of such a loop under ϕ is also nearly a planar loop. We select a point p_0 and travel along the loop. Based on Lemma 1, we can choose any coordinate system and the winding number will not change. Thus, for simplicity, we choose the eigenframe at the start point p_0 to be coordinate system. Therefore, the quaternion for p_0 is $\mathbf{1}$. Since the major eigenvector field is constant along the loop, the quaternions corresponding to the eigenframes along the loop have the form $w + x\mathbf{i}$, i.e., no $\mathbf{j}$ and $\mathbf{k}$ components. Thus, when returning to p_0, the quaternion corresponding to p_0 must be $\pm\mathbf{1}$ or $\pm\mathbf{i}$. When the region R contains no singularity, the winding number is $\mathbf{1}$. Otherwise, it is $\mathbf{i}$ if the singularity contained in R is a wedge or $-\mathbf{i}$ if the singularity is a trisector.

Similarly, in a planar region, the winding number is $\mathbf{1}$ if the region contains no singularity, and is $\mathbf{k}$ or $-\mathbf{k}$ if the singularity is a wedge or a trisector, respectively. □

Corollary 8. *Given a 3D tensor field $T(x,y,z)$ and a topological disk R free of self-intersections, assume that R contains only one degenerate point inside. If furthermore the normal to the surface R is nowhere perpendicular to the dominant eigenvector field, then the winding number of the boundary ∂R is the same as the index of the degenerate point.*

Proof. Given any point p in R, there exists a sufficiently small neighborhood U_p such that Theorem 7 is satisfied. These neighborhoods give an open cover of R. Since R is finite and closed, any of its open covers has a finite subcover [27]. Consequently, we can find a finite neighborhood U_1, U_2, ... U_m for some $m > 0$ such that their union covers R. In Addition, ∂R, a loop, is covered by U_1, ... U_m. It is thus possible to decompose ∂R as the union of a number of closed curves, each of which is inside one such neighborhood U_k for some $1 \le k \le m$. Therefore, the winding number of ∂R is the product of the winding numbers of each of such closed curves (Lemma 5). Since R is nowhere perpendicular to the dominant eigenvector field, the dot product between surface normals (chosen consistently over R) and the dominant eigenvector field over R is either always positive or always negative.

Since R contains only one degenerate point, we can select the closed curves in the open cover such that the degenerate point is inside only one topological disk bounded by the closed curves. For this curve, the winding number is either $\mathbf{i}$, $-\mathbf{i}$, $\mathbf{k}$, or $-\mathbf{k}$ while for the other closed curves, the winding number is $\mathbf{1}$. Thus, the winding number of ∂R is $\pm\mathbf{i}$ or $\pm\mathbf{k}$ due to Lemma 5. □

Fig. 15: The two types of Reidemeister moves that can reduce the number of crossing points in a link diagram.

B Jones Polynomial Computation

In this section, we provide some detail on the technique of computing the Jones polynomials [19], which we implement in our system. Recall that Jones polynomial of a given curve network is defined in terms of the link diagram of curve network, though it is an invariant as it does not depend on the actual choice of the plane onto which the curve network is projected.

As the Jones polynomial is defined recursively, computing it is an NP-hard problem in terms of the number of crossing points in the link diagram. Livingston [19] provides an approximation algorithm by involving the *Reidemeister moves* (Figure 15), which can reduce the number of crossing points without changing the polynomial itself. Note that the reconnection operations in the definition of the Jones polynomials (Figure 10 (a-2.1 and a-2.2)) of a curve network generates two new curve networks, each of which has one fewer crossing points than the original curve network. However, the Jones polynomials of the two new networks are usually different from that of the original one, hence the exponential growth of the computation time in terms of the number of crossing points in the original curve network.

We follow closely the technique of Livingston [19]. Given a degenerate loop in the 3D space, we apply the principal component analysis on the points on the loop, which gives us a new coordinate system. We next project the curve onto the XY-plane of the new coordinate system and ensure we have a regular projection where there are no overlapping edges and no three points projected to the same point on the plane [19]. If it is not a regular projection, we apply a small but random 3D rotation to the coordinate system from the principal component analysis. Since irregular projections are structurally unstable, an arbitrarily small perturbation in the coordination system can usually generate a regular projection. We then construct the link diagram by tracing the crossings on the projected curve. Since the complexity of the Jones polynomial computation is $O(2^n)$ for n crossing points, we simplify the link diagram by reducing the number of crossings points with types I and II Reidemeister moves. This involves the computation of *braid groups*, and we refer our readers to [19] for more detail on this part of the algorithm. Lastly, we compute the Jones polynomial of the simplified curve network by applying the first and second type of simplification rules [19]. We iteratively perform the following two steps. First, any loop in the network free of crossing points with the rest of the networks is removed. When no such loop exists in the remaining network, we remove a crossing with two local reconnection. This leads to two new networks, which are sent to the same routine to compute their respective Jones polynomial. This recursion will eventually lead to the Jones polynomial of the original curve network. Note that we only compute the Jones polynomial for individual degenerate loops for

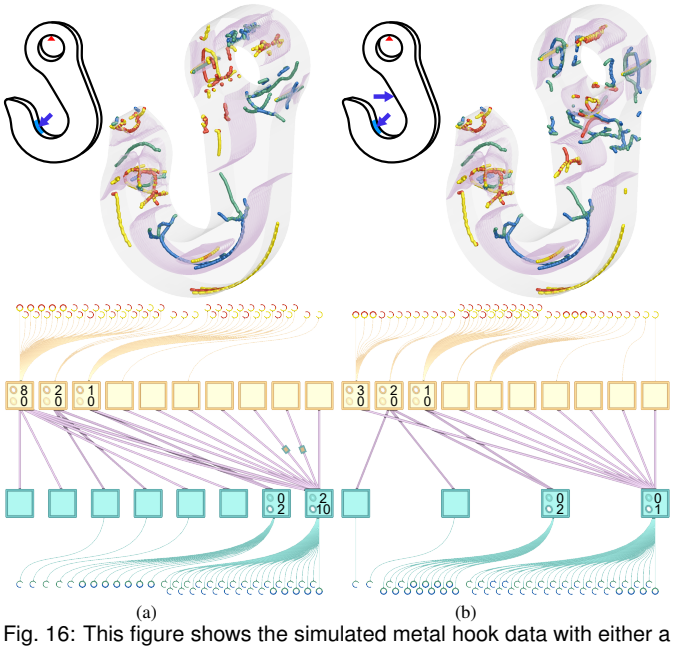

(a) (b)

Fig. 16: This figure shows the simulated metal hook data with either a single-load scenario (a) or a multi-load scenario (b).

knot identification and classification, even though the computation of the Jones polynomial of a loop may result in a curve network in the middle of the computation due to the simplification rules. Finally, when the Jones polynomial is not a constant, we regard the degenerate loop as a knot and add $*$ to the corresponding node in the topological graph.

C Metal Hook

Metal hooks are essential to the lifting mechanism used in construction and transportation engineering. They are often used to lift or pull different kinds of goods that are of varying sizes and shapes. To be able to create cost-effective designs for these hooks, it is important to evaluate their use under different loading conditions. Here we contrast two types of loading conditions for the metal hook example published in SIMULIA 2020. The first type loads the hook from one angle that is shifted to the left from the vertical direction with 1 kN and the second type adds a load pulling in the horizontal direction with 1 kN. The latter simulates a use where the hook carries more than one load. We note that the two scenarios produce very different numbers of regions and degenerate curves. The Betti numbers for the single load scenario are higher for the planar and the linear regions. This was not expected due to the simple load and could not be observed without the topological graph. Moreover, for the second scenario with two loads, there is no region containment as observed for the first scenario in which two planar regions each contains a linear region. This comparison inspires more testing to corroborate the general practice where multiple loads are sometimes applied to ensure little rotational movement of the hook to avoid swinging or tipping.

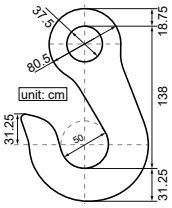

D Eight Pile Group Foundation with Cap

Pile groups are effective foundation structures that support buildings or bridges [4]. Figure 17 illustrates an eight pile group. Knowing how the load distributes and how the material deforms is important to structure integrity evaluation and maintenance scheduling. The most common material used for these pile groups is concrete which is of crushed stones, sand and water. The mixing causes the concrete to have different Poisson's ratios; that is, a pile group may have a range of Poisson's ratios for its piles. Here we contrast two cases where the variation of Poisson's ratios is different. The first case has 0.13 for the center 4 piles and 0.20 for the 4 piles on the ends, while the second increases the Poisson's ratios for the middle 4 piles to 0.24. The latter

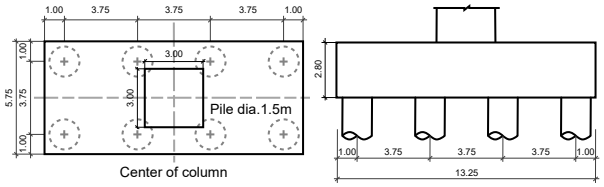

Fig. 17: In this eight pile group, there is a cap that is $13.25 \times 5.75 \times 2.80$ volume meters on top of the piles. Each pile has a diameter of 1.5 meters. The cap is attached to the piles with no movement allowed. The ends of the piles are fixed.

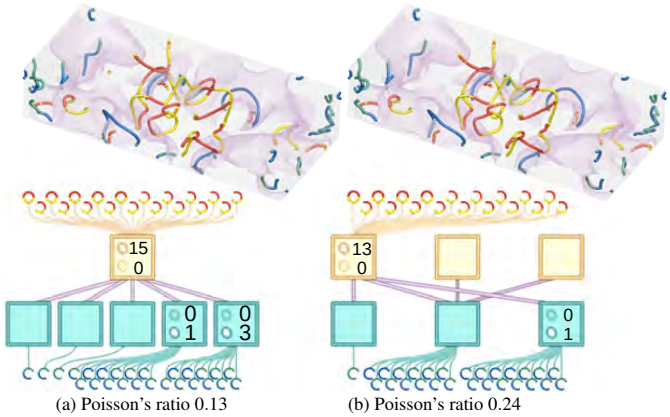

(a) Poisson's ratio 0.13 (b) Poisson's ratio 0.24

Fig. 18: Tensor field topology and its topological graph for the pile cap in an eight pile group foundation. The first case (left) has its four center piles at a lower Poisson's ratio (0.13) and its four piles at the ends at a higher Poisson's ratio (0.20). The second case (right) has its four center piles at a higher Poisson's ratio (0.24) while maintaining the Poisson's ratios of the four piles at the ends at 0.20.

simulates a more incompressible center than the ends and the former is the reverse. We add a vertical load, 1000 kN, at the center top (3×3 square meters) and a small periodic loading to the sides of the pile cap.

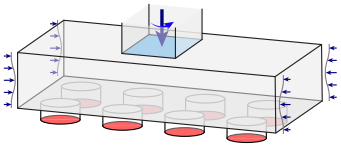

Using the topological graphs (Figure 18), we can observe that there are more linear regions representing extensions than the planar regions representing compression for the first case while there are the same number of linear and planar regions in the second case. The Betti numbers are higher for the regions in the first case. Conjectures such as having a more incompressible center group, i.e., higher Poisson's ratio for the center piles, leads to a more uniform material behavior for the cap become plausible; however, only extensive studies can warrant these statements. Our topological graphs can aid in establishing these conjectures to provide practical guidance on the pile arrangement for long-lasting concrete foundations.

E Additional O-ring Analysis

In this section, we add some discussions on the results from varying the periodicity of loading on the O-ring. We provide a group of examples while varying p and q in Equation 8.

Our results are shown in Figure 19 as an array of sub-figures. Along the vertical direction, the value of p increases and along the horizontal direction, q increases. We first note that for high values of p and q, the topological graphs are more complex in terms of increased number of regions and degenerate curves. For $q = 1$ which is shown in the left-most column, there is no region containment. For $q = 2$, a new planar region appears for each value of p, and it resides inside the green region. One of the straight purple edges representing the neutral surfaces is encoded with the glyph that shows containment. For $q = 3$, this planar

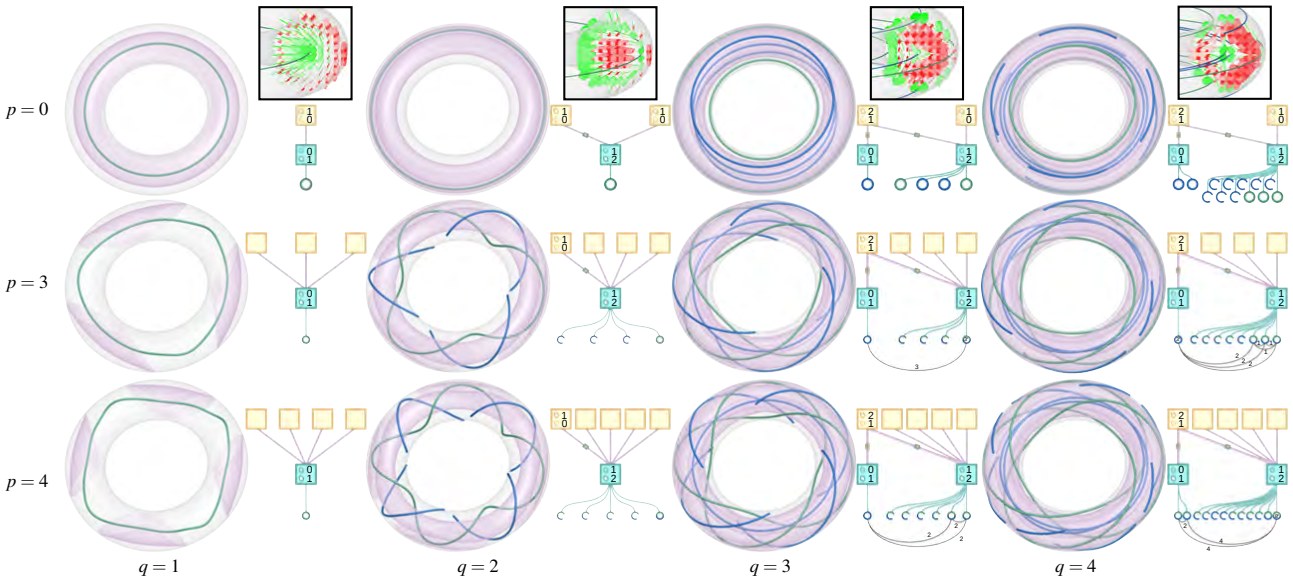

Fig. 19: We evaluate the compression force of $p = 0, 3, 4$, $q = 1, 3, 4$, and $\alpha = 0.3$. For each scenario, we show the tensor field features on the left and the topological graph on the right. As p increases, the number of the features such as degenerate curves increases due to the periodicity of the compression force. On the other hand, As q increases, trisector degenerate curves start to appear. We also show the glyphs on a cross-section for the case of $p = 0$ to indicate the eigenvector fields.

region starts to host a linear region, which itself contains another planar region. The appearance of the nested regions is a direct response of material deformation to the boundary condition change. Furthermore, linking among linear degenerate curves starts to form. In particular, for $p = q = 3$, a trefoil appears. As q increases to 4, this trefoil breaks and many more degenerate curves appear and link. For $p = q = 4$, a knot with a Writhe number 8 appears. More complex linking and knotting behaviors are expected as p and q increase. During this deformation, degenerate curves that are either extension or compression dominant will intertwine with each other. The knottiness may indicate a match of the physical domain boundary with the high stress loading spots that enclose the same material deformation behavior entirely inside the physical domain. In future work, we plan to continue with the experiments for many more scenarios to detect patterns and mathematical reasons.